The Astrophysical Journal, 862:40 (16pp), 2018 July 20 https://doi.org/10.3847/1538-4357/aaccdf
© 2018. The American Astronomical Society. All rights reserved.

Probing Cosmology with Dark Matter Halo Sparsity Using X-Ray Cluster Mass Measurements

P. S. Corasaniti[1], S. Ettori[2,3], Y. Rasera[1], M. Sereno[2,4], S. Amodeo[5], M.-A. Breton[1], V. Ghirardini[2,4], and D. Eckert[6]
[1] LUTH, Observatoire de Paris, PSL Research University, CNRS, Université Paris Diderot, Sorbonne Paris Cité, 5 Place Jules Janssen, F-92195 Meudon, France
[2] INAF, Osservatorio Astronomico di Bologna, via Piero Gobetti 93/3, I-40129 Bologna, Italy
[3] INFN, Sezione di Bologna, viale Berti Pichat 6/2, I-40127 Bologna, Italy
[4] Dipartimento di Fisica e Astronomia, Università di Bologna, via Piero Gobetti 93/2, I-40129 Bologna, Italy
[5] LERMA, Observatoire de Paris, PSL Research University, CNRS, Sorbonne Université, UPMC Univ. Paris 6, F-75014 Paris, France
[6] Max-Planck-Institute for Extraterrestrial Physics (MPE), Giessenbachstrasse 1, D-85748 Garching, Germany
Received 2017 October 31; revised 2018 June 12; accepted 2018 June 12; published 2018 July 20

Abstract

We present a new cosmological probe for galaxy clusters, the halo sparsity. This characterizes halos in terms of the ratio of halo masses measured at two different radii and carries cosmological information encoded in the halo mass profile. Building on the work of Balmes et al., we test the properties of the sparsity using halo catalogs from a numerical N-body simulation of $(2.6\ \mathrm{Gpc}\ h^{-1})^3$ volume with 4096^3 particles. We show that at a given redshift the average sparsity can be predicted from prior knowledge of the halo mass function. This provides a quantitative framework to infer cosmological parameter constraints using measurements of the sparsity of galaxy clusters. We show this point by performing a likelihood analysis of synthetic data sets with no systematics, from which we recover the input fiducial cosmology. We also perform a preliminary analysis of potential systematic errors and provide an estimate of the impact of baryonic effects on sparsity measurements. We evaluate the sparsity for a sample of 104 clusters with hydrostatic masses from X-ray observations and derive constraints on the cosmic matter density Ω_m and the normalization amplitude of density fluctuations at the 8 Mpc h^{-1} scale, σ_8. Assuming no systematics, we find $\Omega_m = 0.42 \pm 0.17$ and $\sigma_8 = 0.80 \pm 0.31$ at 1σ, corresponding to $S_8 \equiv \sigma_8\sqrt{\Omega_m} = 0.48 \pm 0.11$. Future cluster surveys may provide opportunities for precise measurements of the sparsity. A sample of a few hundred clusters with mass estimate errors at the few percent level can provide competitive cosmological parameter constraints complementary to those inferred from other cosmic probes.

Key words: cosmological parameters – cosmology: theory – methods: numerical – X-rays: galaxies: clusters

1. Introduction

In the standard bottom-up scenario of cosmic structure formation, initially small dark matter (DM) density fluctuations grow under gravitational instability to eventually form at later times virialized stable objects, the halos. It is inside these gravitationally bounded clumps of DM that baryonic gas falls in to form the visible structures we observe in the universe. Today, the most massive halos host large clusters of galaxies resulting from the hierarchical merging process of lower-mass halos formed at earlier times. Since their assembly depends on the matter content of the universe, the state of cosmic expansion, and the initial distribution of matter density fluctuations, there is a consensus that observations of galaxy clusters can provide a wealth of cosmological information (see, e.g., Allen et al. 2011; Kravtsov & Borgani 2012, for a review of galaxy cluster cosmology).

Galaxy clusters can be observed through a variety of probes, such as the detection of the X-ray emission of the intracluster gas (e.g., Vikhlinin et al. 2005; Ebeling et al. 2010; Piffaretti et al. 2011; Pierre et al. 2016), the Sunyaev–Zel'dovich effect in the microwave (e.g., Staniszewski et al. 2009; Menanteau et al. 2013; Reichardt et al. 2013; Planck Collaboration et al. 2016b), the distribution of the member galaxies in the optical and IR bands (Koester et al. 2007; Rykoff et al. 2014), and the distortion of the background galaxies induced by the halo gravitational potential (e.g., Umetsu et al. 2011; Hoekstra et al. 2012; Postman et al. 2012).

Due to the highly nonlinear nature of the gravitational collapse driving the formation of DM halos, theoretical model predictions, which are necessary to interpret the data and infer cosmological parameter constraints, have been mainly obtained through cosmological simulations. A remarkable result of these studies is the fact that DM halos exhibit a universal density profile well approximated by the Navarro–Frenk–White formula (Navarro et al. 1997). This entirely characterizes the halo profile in terms of the halo mass M and the concentration parameter c. Numerical simulations have shown that the concentration encodes cosmological information. In particular, it has been found that the median concentration of an ensemble of halos is a power-law function of the halo mass with the overall amplitude of the relation varying with redshift and cosmology (see, e.g., Bullock et al. 2001; Zhao et al. 2003; Dolag et al. 2004; Zhao et al. 2009; Giocoli et al. 2012). This has suggested that estimates of the concentration and halo mass from a sample of galaxy clusters can provide constraints on cosmological models (see, e.g., Ettori et al. 2010, for a cosmological data analysis using cluster concentration–mass measurements).

However, several factors can limit the use of the cluster concentration as cosmological proxy. On the one hand, astrophysical effects may alter the original c–M relation and introduce a systematic bias into the cosmological analysis (see, e.g., Duffy et al. 2010; Mead et al. 2010; King & Mead 2011). On the other hand, theoretical model predictions, despite recent progress (see, e.g., Correa et al. 2015; Diemer & Kravtsov 2015; Klypin et al. 2016; Ludlow et al. 2016; Renneby et al. 2017), have yet to converge into a single model capable of reproducing the ensemble of numerical results currently

available for different cosmological scenarios (Meneghetti & Rasia 2013).

Another limiting factor may result from the large intrinsic dispersion of the halo concentration. *N*-body simulation studies have found a significant scatter of the concentration at fixed halo mass (Bullock et al. 2001; Wechsler et al. 2002). For example, Maccio et al. (2007) have found $\sigma_{\ln c} \approx 0.25$, while Bhattacharya et al. (2013) quote a scatter $\sigma_{\ln c} \approx 0.33$. A similar result has been found in Diemer & Kravtsov (2015), which quotes $\sigma_{\ln c} \approx 0.37$, while a smaller value was only found for a sample of relaxed halos. Accounting for such a large intrinsic dispersion may strongly relax cosmological parameter constraints from measurements of the concentration–mass relation.

A further point of concern is the case of very massive clusters. These are often easier to detect because they are very luminous and rich. Nonetheless, because of their recent formation, they are also more likely to be perturbed by the presence of other structures that are still in the process of merging with the main DM halo. In such a case, the halo density profile may deviate from the NFW formula, and the concentration parameter no longer encodes information of the halo mass distribution and its cosmological dependence.

Finally, the measurement of the mass–concentration relation is strongly affected by selection effects as shown by Sereno et al. (2015).

In Balmes et al. (2014), two of the authors have introduced the concept of halo *sparsity*, a directly measurable proxy of the DM halo mass profile that overcomes most of the limitations described above. In this work, we present a detailed study of the validity of the halo sparsity as a new cosmological probe. As a proof-of-concept application, we specifically focus on sparsity measurements based on hydrostatic mass estimates from X-ray cluster observations. We show that the redshift evolution of the average halo sparsity carries cosmological information that can be retrieved from prior knowledge of the halo mass function. To this purpose we perform a likelihood analysis over a set of ideal sparsity data with no systematic errors from which we recover the input fiducial cosmology. We discuss various sources of systematic uncertainty. Using results from state-of-the-art simulations of galaxy clusters, we show that mass bias effects due to baryonic feedback processes alter the sparsity of massive systems at the few percent level. When analyzing cluster sparsity, this source of systematic error is therefore subdominant with respect to that affecting mass estimates from currently available cluster data sets. As a first cosmological application, we perform a cosmological parameter inference analysis of sparsity measurements based on hydrostatic mass estimates of a sample of X-ray clusters from *XMM* and *Chandra* observations.

The article is organized as follows. In Section 2, we review the basic properties of the halo sparsity and test its validity as a cosmological proxy. In Section 3, we discuss several sources of systematic errors that can affect the sparsity data analysis. In Section 4, we present the cosmological parameter constraints inferred from sparsity measurements of a sample of X-ray clusters. In Section 5, we perform a cosmological parameter forecast for sparsity data expected from future X-ray cluster surveys. Finally, in Section 6 we present our conclusions.

2. DM Halo Sparsity

2.1. Definition and Properties

The sparsity of a halo is defined as the ratio of the halo mass enclosing two different overdensities Δ_1 and Δ_2 (Balmes et al. 2014):

$$s_{\Delta_1,\Delta_2} \equiv \frac{M_{\Delta_1}}{M_{\Delta_2}}, \tag{1}$$

where $\Delta_1 < \Delta_2$ and M_Δ is the mass enclosed in a sphere of radius r_Δ containing an overdensity Δ with respect to the critical density ρ_c or the mean background density ρ_m. In the following we will consider ρ_c; however, as shown in Balmes et al. (2014), the general properties of the sparsity are independent of such a choice. Notice that from Equation (1) we can also interpret the sparsity of a halo as a measure of the mass excess between r_{Δ_1} and r_{Δ_2} ($\Delta M = M_{\Delta_1} - M_{\Delta_2}$) relative to the mass enclosed in the inner radius r_{Δ_2}, i.e., $s_{\Delta_1,\Delta_2} = \Delta M / M_{\Delta_2} + 1$.

It is easy to show that there is a one-to-one correspondence between the halo sparsity and the concentration parameter (assuming that the halo follows the NFW profile). For instance, to conform with the standard definition of concentration, let us set $\Delta_1 = 200$ and let Δ_2 be equal to Δ; then, using the NFW formula, we can write the sparsity as

$$s_\Delta^{-1} \equiv x_\Delta^3 \frac{\Delta}{200} = \frac{\ln(1 + c_{200}\, x_\Delta) - \frac{c_{200}\, x_\Delta}{1 + c_{200}\, x_\Delta}}{\ln(1 + c_{200}) - \frac{c_{200}}{1 + c_{200}}}, \tag{2}$$

where $x_\Delta = r_\Delta / r_{200}$ and $c_{200} = r_{200}/r_s$, with r_s the scale radius of the NFW profile. For a given set of values of the concentration c and overdensity Δ, the above equation can be solved numerically to obtain x_Δ and thus the corresponding value of s_Δ. However, notice that in defining the sparsity as in Equation (1) no explicit assumption has been made concerning the form of the halo density profile. Balmes et al. (2014) have shown that this is sufficient to characterize the mass profiles of halos even when their density profile deviates from NFW.

A key feature of the halo sparsity is the fact that its ensemble average value at a given redshift is nearly independent of the halo mass M_{Δ_1} (even if some of the halos in the ensemble have profiles that deviate from NFW) but depends on the underlying cosmological model with a scatter that is much smaller than that of the halo concentration. Because of this, it can provide a robust cosmological proxy, without requiring any modeling of the halo density profile.

Another important characteristic of the halo sparsity is that its independence on M_{Δ_1} implies that the ensemble average value can be predicted from prior knowledge of the halo mass function at two different mass overdensities. In fact, let us consider the equality

$$\frac{dn}{dM_{\Delta_2}} = \frac{dn}{dM_{\Delta_1}} \frac{dM_{\Delta_1}}{dM_{\Delta_2}} = \frac{dn}{dM_{\Delta_1}} s_{\Delta_1,\Delta_2} \frac{d \ln M_{\Delta_1}}{d \ln M_{\Delta_2}}, \tag{3}$$

where dn/dM_{Δ_1} and dn/dM_{Δ_2} are the mass functions at Δ_1 and Δ_2, respectively. We can rearrange the above relation and integrate over the halo ensemble mass range to derive the relation between the average inverse halo masses at two different overdensities. Since the sparsity is independent of the halo mass, it can be taken out of the integration on the

right-hand side such that

$$\int_{M_{\Delta_2}^{\min}}^{M_{\Delta_2}^{\max}} \frac{dn}{dM_{\Delta_2}} d\ln M_{\Delta_2} = \langle s_{\Delta_1,\Delta_2}\rangle \int_{\langle s_{\Delta_1,\Delta_2}\rangle M_{\Delta_2}^{\min}}^{\langle s_{\Delta_1,\Delta_2}\rangle M_{\Delta_2}^{\max}} \frac{dn}{dM_{\Delta_1}} d\ln M_{\Delta_1}. \quad (4)$$

This equation can be solved numerically for $\langle s_{\Delta_1,\Delta_2}\rangle$ given prior knowledge of dn/dM_{Δ_1} and dn/dM_{Δ_2}, respectively. As shown in Balmes et al. (2014), this reproduces with great accuracy the mean sparsity inferred from N-body halo catalogs. Indeed, this is a direct advantage over predicting the median concentration, since the cosmological and redshift dependences of the mass function are easier to model than the concentration, as they involve a reduced set of assumptions. Moreover, since the sparsity is a mass ratio, it is reasonable to expect that it will be less affected by a constant systematic bias that may affect cluster mass measurements. Also, notice that selection effects can be included in Equation (4) by convolving the integrands with the appropriate selection function. We will discuss both these points in detail in Section 3.

A last remark concerns the choice of Δ_1 and Δ_2 provided that $\Delta_1 < \Delta_2$. As noticed in Balmes et al. (2014), the larger the difference, the greater the amplitude of the cosmological signal. However, the values of Δ_1 and Δ_2 cannot be chosen to be arbitrarily different since the properties of the sparsity discussed above remain valid only in a limited interval that can be determined by physical considerations. A lower bound on Δ_1 can be inferred by the fact that for very small overdensities the identification of a halo as an individual object can be ambiguous, thus suggesting $\Delta_1 \gtrsim 100$. On the other hand, the range of values for Δ_2 can be deduced by the fact that at very large overdensities baryonic processes may alter the DM distribution within the inner core of halos. These are largely subdominant if one conservatively assumes Δ_2 in the range $\Delta_1 < \Delta_2 \lesssim 2000$. Within this interval of values one can set Δ_1 and Δ_2 depending on the availability of optimal mass measurements.

2.2. N-body Simulation Sparsity Tests

In Balmes et al. (2014) the properties of the halo sparsity have been tested using halo catalogs from the Dark Energy Universe Simulations[7] (DEUS) with masses defined with respect to the background density covering the mass range $10^{12} < M_{200\,\mathrm{m}}\ [h^{-1}\,M_\odot] < 10^{15}$.

Here we perform an analysis using halos identified with the Spherical Overdensity (SOD) halo detection algorithm (Lacey & Cole 1994) in one of the simulations of the RayGalGroupSims suite (M.-A. Breton et al. 2018, in preparation) with masses defined with respect to the critical density. Since we are interested in the application to X-ray clusters, we specifically focus on masses at overdensity $\Delta_1 = 500c$ and $\Delta_2 = 1000c$, from which we derive estimates of the halo sparsity $s_{500,1000}$. For completeness, we also consider halo masses measured at $\Delta_1 = 200c$ and show that the properties of the halo sparsity also hold for $s_{200,500}$ and $s_{200,1000}$.

The cosmological model of the RayGalGroupSims simulation considered here is a flat ΛCDM with parameters set consistently with *WMAP* 7 yr data analysis (Komatsu et al. 2011): $\Omega_m = 0.2573$, $\Omega_b = 0.04356$, $h = 0.72$, $n_s = 0.963$, and $\sigma_8 = 0.801$. The simulation consists of a $(2.625\ \mathrm{Gpc}\ h^{-1})^3$ volume with 4096^3 particles corresponding to particle mass resolution $m_p = 1.88 \cdot 10^{10}\ M_\odot h^{-1}$.

Halos are first detected using the SOD algorithm with overdensity set to $\Delta = 200c$ and centered on the location of maximum density. For each halo we computed SOD masses at $\Delta = 200c$, $500c$, and $1000c$ and estimated the corresponding halo sparsities. In order to avoid mass resolution effects, we have taken a conservative mass cut and considered only halos with more than 10^4 particles.

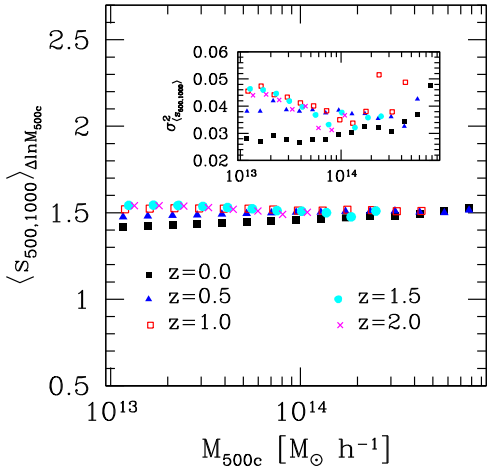


Figure 1. Average halo sparsity as a function of M_{500c} from SOD halo catalogs at $z = 0$ (black filled squares), $z = 0.5$ (blue filled triangles), 1.0 (red open squares), 1.5 (cyan filled circles), and 2.0 (magenta crosses) in mass bins of size $\Delta \ln M_{500c} = 0.3$. The inset plot shows the variance of the halo sparsity in the same mass bins as a function of M_{500c} for the different redshifts.

In Figure 1 we plot the average halo sparsity $\langle s_{500,1000}\rangle_{\Delta \ln M_{500c}}$ in mass bins of size $\Delta \ln M_{500c} = 0.3$ (containing more than 20 halos) as a function of M_{500c} at $z = 0$, 0.5, 1.0, 1.5, and 2.0, while in the inset plot we show the associated variance. As we can see, $\langle s_{500,1000}\rangle_{\Delta \ln M_{500c}}$ remains constant to very good approximation across the full mass and redshift range. As far as the scatter is concerned, we find the standard deviation to be at the $\lesssim$20% level, consistent with the findings of Balmes et al. (2014).

Let us now test the validity of Equation (4) in predicting the redshift evolution of the ensemble average sparsity. In Figure 2, the black circles are the average sparsity values obtained from the RayGalGroupSims halo catalogs at $z = 0$, 0.5, 0.66, 1.0, 1.14, 1.5, and 2.0. These have been computed for each halo catalog by averaging the sparsity of halos with $M_{500c} \gtrsim 10^{13}\,M_\odot\ h^{-1}$. The magenta squares are the average sparsity values at the redshifts of the halo catalogs obtained by solving Equation (4), where we have assumed the Sheth–Tormen (ST) formula (Sheth & Tormen 1999) with coefficients best-fitting the numerical halo mass functions at $\Delta_1 = 500c$ and $\Delta_2 = 1000c$ (see the Appendix for a detailed description of the mass function calibration). As we can see in Figure 2, the predictions from Equation (4) overlap with the average sparsity values directly estimated from the halos in the simulation catalogs with relative differences at the <0.1% level.[8]

[7] http://www.deus-consortium.org/deus-data/

[8] In solving Equation (4) we have set $M_{1000c}^{\min} = 2 \cdot 10^{13}\,M_\odot\ h^{-1}$ consistently with the mass limit of our halo catalogs, while the upper limit of the integration interval can be set to an arbitrarily large number. Nevertheless, as the average sparsity remains approximately constant with mass, we have verified that the solution of Equation (4) is largely independent of the specific choice of $M_{1000c}^{\min}$.

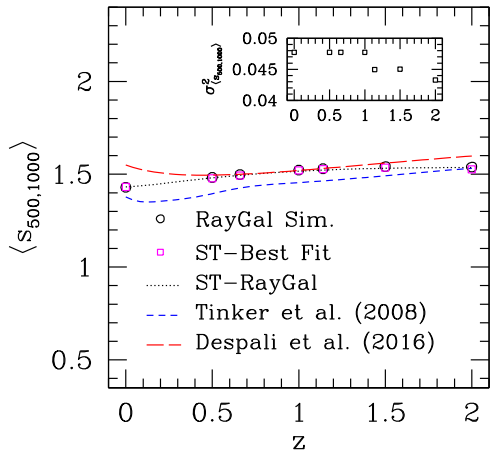


Figure 2. Average sparsity as a function of redshift for halos with $M_{500c} > 10^{13}\,M_\odot\,h^{-1}$. The black circles correspond to the average sparsity measured from the halo catalogs at the redshift snapshots of the RayGalGroupSims run. The magenta squares correspond to the average sparsity prediction obtained by solving Equation (4) assuming an ST mass function with coefficients best-fitting the halo mass function of the RayGalGroupSims halo catalogs at M_{500c} and M_{1000c}. The black dotted line corresponds to the prediction from Equation (4) using the ST-RayGal mass function, while the blue short-dashed line and the red long-dashed line correspond to the predictions obtained by assuming the mass function from Tinker et al. (2008) and Despali et al. (2016), respectively. The inset plot shows the variance of the halo sparsity from the SOD halo catalogs with $M_{500c} \gtrsim 10^{13}\,M_\odot\,h^{-1}$ at the different redshift snapshots.

In order to interpolate predictions of the sparsity at redshifts other than those tested by the simulation snapshots, we have performed a quadratic fit of the ST best-fit coefficients as a function of $x \equiv \log_{10}(\Delta_c/\Delta_{\rm vir}(z))$ for $\Delta_c = 500$ and 1000; see Equations (16)–(17) in the Appendix. As suggested by Despali et al. (2016), parameterizing the ST coefficients in terms of x aims to capture the redshift and cosmology dependence of the mass function, though from the work of Courtin et al. (2011) it is clear that this may not be sufficient to model dependencies beyond the ΛCDM scenario. Hereafter, we will refer to the ST formula with coefficients given by Equations (16) and (17) as the ST-RayGal mass function; the corresponding average sparsity prediction from Equation (4) is shown in Figure 2 as a black dotted line. We find differences with respect to the N-body measurements to be at the subpercent level.

In Figure 2 we also plot the average sparsity prediction from Equation (4) obtained by assuming the mass function from Tinker et al. (2008) and Despali et al. (2016). In the former case we can see systematic deviations up to the ∼10% level with respect to the N-body estimates that decrease from low to high redshifts. In the latter case differences are within the 1% level in the range $0.5 < z < 1.5$, while they increase up to the ∼10% level at lower and higher redshifts. Such discrepancies are due to differences in the parameterizations of the halo mass function, which have been calibrated to halo catalogs from simulations of different cosmological models, volumes, and mass resolutions.

Compared to the simulations used in Tinker et al. (2008) and Despali et al. (2016), the RayGalGroupSims simulation covers a larger volume with greater mass resolution. This provides a better calibration of the ST formulae. As can be seen in Figure 14 in the Appendix, we find logarithmic differences well within the 5% level. On the other hand, it is worth remarking that we have tested the validity of the ST-RayGal mass function to a set of cosmological simulations with parameters that are not too different from those of the ΛCDM best-fit model to the *WMAP* 7 yr data (see discussion at the end of the Appendix). Consequently, we are not guaranteed that the ST-RayGal parameterization can fully capture the cosmological parameter dependence of the halo mass function and hence that of the halo sparsity for parameter values that are far from the concordance ΛCDM model. Such uncertainty can indeed introduce systematic errors in the sparsity analysis, a point that we will discuss in detail in Section 3. Here, we are not in a position to solve this issue in a conclusive manner. Hence, we simply opt to quote the results obtained assuming the ST-RayGal parameterization and that from Despali et al. (2016). We will refer to the latter case as ST-Despali.

The properties of the halo sparsity summarized by the trends shown in Figures 1 and 2 also hold for other sparsity definitions. This can be seen in Figure 3, where we plot $\langle s_{200,500}\rangle$ and $\langle s_{200,1000}\rangle$ as a function of M_{200c} and redshift, respectively. These plots suggest that sparsity estimations from mass measurements at $\Delta = 200c$, such as those provided by gravitational lensing observations that probe clusters at larger radii than X-ray measurements, can also provide a viable proxy of the mass distribution in clusters.

2.3. Cosmological Parameter Dependence

The dependence of the halo sparsity on the underlying cosmological model has been studied in Balmes et al. (2014) using N-body halo catalogs from DEUS project simulations (Alimi et al. 2010; Rasera et al. 2010; Courtin et al. 2011). Balmes et al. (2014) have shown that the average value of the sparsity at a given redshift correlates with the linear growth factor of the underlying cosmological model. This can be qualitatively understood in terms of the relation between the growth of structures and the mass assembly of halos. In particular, at any given time, models that form structures earlier will assemble on average more halo mass at large overdensities (inner radii) than those that form structures at later times, thus resulting in smaller values of the average sparsity. In terms of the cosmological model parameters, this implies, for instance, that the larger the cosmic matter density Ω_m or the amplitude of the fluctuations on the 8 Mpc h^{-1} scale σ_8, the smaller the average sparsity value.

Here, we do not intend to repeat the analysis of Balmes et al. (2014); instead, we use Equation (4) to evaluate the relative change of the average sparsity with respect to a fiducial cosmological model for a positive variation of the cosmological parameters.

We assume as fiducial cosmology a flat ΛCDM model with parameters set to the best-fit values from the *Planck* cosmological data analysis of cosmic microwave background (CMB) anisotropy spectra (TT, TE, EE + lowP; Planck Collaboration et al. 2016a): $\Omega_m = 0.3156$, $\Omega_b h^2 = 0.02225$, $h = 0.6727$, $\sigma_8 = 0.831$, $n_s = 0.9645$.

We compute $\langle s_{500,1000}\rangle$ from Equation (4) assuming the ST-RayGal and ST-Despali mass functions, respectively.[9]

In Figure 4 we plot $\Delta\langle s_{500,1000}\rangle/\langle s_{500,1000}\rangle_{\rm fid}$ as a function of redshift in the case of the ST-RayGal mass function (top panel)

[9] In computing the mass function, we evaluate the linear matter power spectrum of the underlying cosmological model using the approximated formulae from Eisenstein & Hu (1999). We have verified that using power spectra from numerical solutions of linear perturbation equations, such as those given by the CAMB code (Lewis et al. 2000), leads to subpercent difference in the predicted value of the average sparsity.

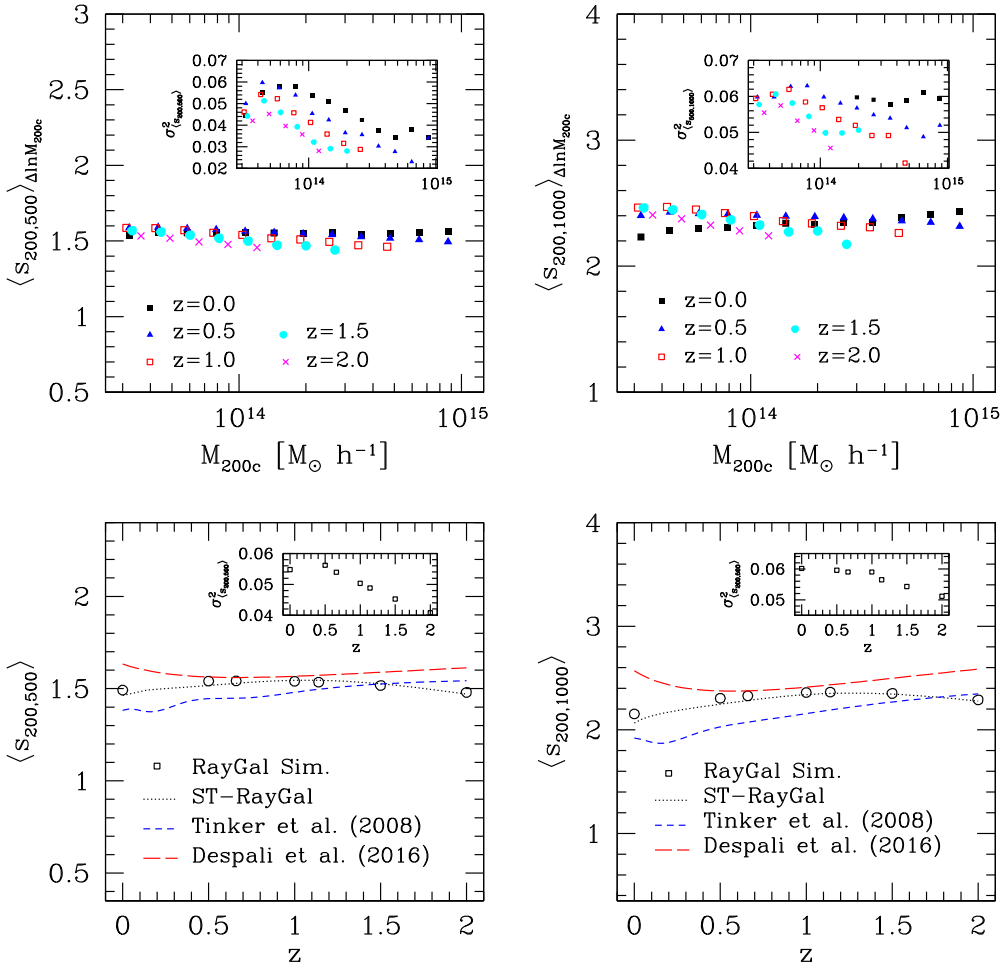


Figure 3. Top panels: average halo sparsity $\langle s_{200,500}\rangle$ (left panel) and $\langle s_{200,1000}\rangle$ as a function of M_{200c} at $z = 0$, 0.5, 1, 1.5, and 2.0 (legend as in Figure 1) in mass bins of size $\Delta \ln M_{200c} = 0.3$. The inset plot shows the variance of the halo sparsity in the same mass bins as a function of M_{200c} for the different redshifts. Bottom panels: average halo sparsity $\langle s_{200,500}\rangle$ (left panel) and $\langle s_{200,1000}\rangle$ as a function of redshift for halos (legend as in Figure 2) with $M_{500c} > 10^{13}\, M_\odot\, h^{-1}$ consistently with the mass cut adopted for the $s_{500,1000}$ case. The inset plot shows the variance of the halo sparsity at the different redshift snapshots.

and ST-Despali mass function (bottom panel). Independently of the adopted mass function parameterization, we can see that the variation of the average sparsity is negative for a positive variation of the cosmological parameters, except $\Omega_b h^2$. This is essentially because increasing the value of σ_8, Ω_m, n_s, and h causes structures to form at earlier times and consequently assemble more halo mass at larger overdensities, which results in smaller values of the average sparsity. This is not the case for positive variations of $\Omega_b h^2$. In fact, as we have assumed a flat geometry, increasing the value of $\Omega_b h^2$ corresponds to decreasing the value of Ω_m at constant h. In such a case, structures form later than in models with smaller values of $\Omega_b h^2$, and halos assemble on average less mass at larger overdensities, thus leading to larger values of the average sparsity.

The trends shown in Figure 4 provide an estimate of the sensitivity of the average sparsity to the different cosmological parameters. In the ST-RayGal case we can see that a change in the value of σ_8 produces the largest variation of the average sparsity in the redshift range $0 < z \lesssim 1$. At higher redshifts a change in the value of n_s causes the largest variation, while Ω_m, h, and $\Omega_b h^2$ have smaller effects. A similar trend occurs in the ST-Despali case, though with different amplitudes for the different parameters. Overall, we can see that measurements of the average sparsity are most sensitive to $S_8 = \sigma_8\sqrt{\Omega_m}$; consequently, we can expect constraints on Ω_m and σ_8 to be degenerate along curves of constant S_8 values.

It is worth noticing that the variations of the average sparsity predicted by the ST-Despali mass function are slightly larger in amplitude than those from the ST-RayGal. This suggests that cosmological constraints inferred by a sparsity analysis based on the ST-Despali mass function will provide systematically tighter bounds than those inferred assuming the ST-RayGal parameterization. As already mentioned at the end of Section 2.2, the uncertainties in the modeling of the halo mass function may induce a systematic error in the cosmological analysis of sparsity measurements. We will discuss this in detail in Section 3.

2.4. Synthetic Data Analysis

We now check the validity of the average sparsity as cosmological proxy. To this purpose we generate a set of synthetic average sparsity data and perform a cosmological parameter likelihood analysis to test whether we retrieve the input parameter values of the fiducial cosmology. As proof of concept, here we limit ourselves to ideal sparsity measurements and neglect any source of systematic uncertainty. Our goal is to show that the sparsity provides a viable cosmological observable.

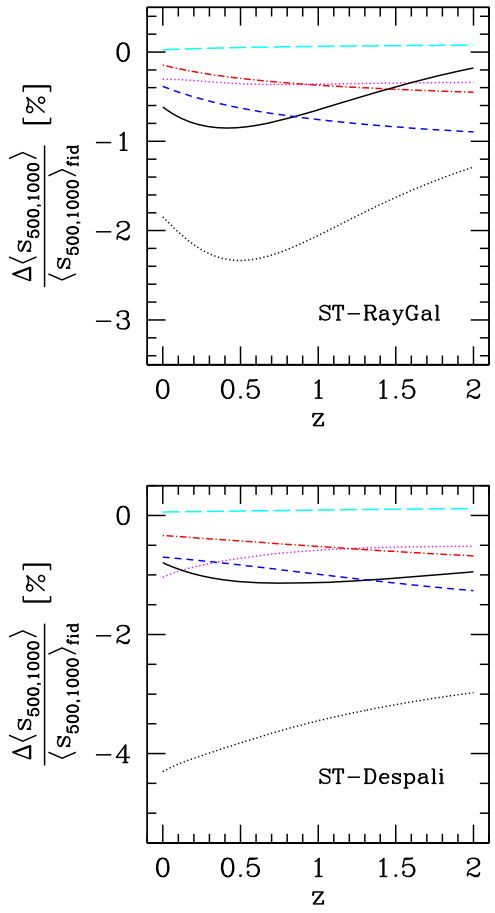


Figure 4. Relative variation of the average halo sparsity as a function of redshift for a 5% variation of the cosmological parameters around the fiducial *Planck* values. The various lines represent variations with respect to σ_8 (black solid line), n_s (blue short-dashed line), Ω_m (magenta dotted line), h (red dot-dashed line), $\Omega_b h^2$ (cyan long-dashed line), and $\sigma_8\sqrt{\Omega_m}$ (black dotted line). In the top panel we plot the relative variation of the average sparsity obtained assuming the ST-RayGal mass function in Equation (4), while that assuming the ST-Despali mass function is shown in the bottom panel.

We assume as a fiducial model a flat ΛCDM scenario with parameters set to the *Planck* best-fit values quoted in Section 2.3. We generate a sample of $N = 15$ independent sparsity measurements in redshift bins of size $\Delta z = 0.1$ over the range $0 \leqslant z \leqslant 1.5$ by solving Equation (4) for a given mass function. We consider two separate configurations, one consisting of sparsity measurements with 1% statistical errors and another with 20% errors. This allows us to test whether degrading the statistical uncertainties has an impact in retrieving the fiducial model. We focus the parameter inference on σ_8 and Ω_m, while assuming hard priors on the remaining cosmological parameters. We realize two independent analyses for the ST-RayGal and the ST-Despali mass functions.

We perform a Markov chain Monte Carlo sampling of the likelihood function and evaluate the χ^2:

$$\chi^2(\sigma_8, \Omega_m) = \sum_{i=1}^{N}\left[\frac{\langle s^i_{500,1000}\rangle - \langle s^{\rm th}_{500,1000}(z_i|\sigma_8, \Omega_m)\rangle}{\sigma_{\langle s_{500,1000}\rangle}}\right]^2, \quad (5)$$

where $\langle s^i_{500,1000}\rangle$ is the ith data point in the synthetic catalog at redshift z_i, $\sigma_{\langle s_{500,1000}\rangle}$ is the associated error, and $\langle s^{\rm th}_{500,1000}\rangle$ is the theoretical model prediction given by Equation (4) assuming the same mass function parameterization used to generate the data.

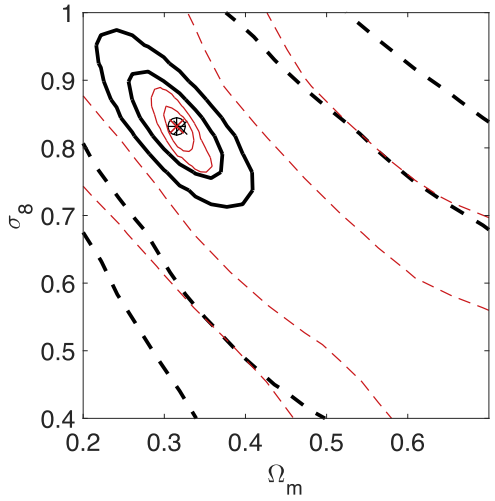


Figure 5. 1σ and 2σ credibility contours in the Ω_m–σ_8 plane obtained in the case of the ST-RayGal mass function (black thick lines) and the ST-Despali mass function (red thin lines). The solid lines correspond to constraints inferred assuming 1% average sparsity errors, while the dashed contours correspond to the case with 20% errors. The black circled plus sign indicates the fiducial model parameters, while the black and red cross markers indicate the best-fit values.

The results are summarized in Figure 5, where we plot the 1σ and 2σ credibility contours in the plane Ω_m–σ_8, which have been inferred assuming the ST-RayGal and ST-Despali mass functions, respectively. In both cases we find the best-fit model parameters to recover the *Planck* fiducial parameters at the subpercent level, independently of the assumed uncertainties on the synthetic data set. On the other hand, we can see that the parameter constraints become much weaker in the case with 20% statistical errors. As expected from the analysis presented in Section 2.3, the analysis of the synthetic data performed using the ST-Despali mass function provides systematically tighter bounds on Ω_m–σ_8 than the ST-RayGal case.

Overall, this suggests that the average sparsity can be used as a cosmic probe. We will discuss extensively in the next section the extent to which systematic errors can contaminate sparsity analyses.

3. Systematic Errors

In this section we present a preliminary evaluation of systematic errors potentially affecting cluster sparsity analyses.

3.1. Mass Function Parameterization

In Section 2.2 we have seen that key to predicting the halo sparsity is the correct modeling of the halo mass function. In particular, we have shown that Equation (4) recovers the average sparsity of the numerical halo catalogs from the RayGalGroupSims simulation provided that the parameterization of the halo mass function for M_{500c} and M_{1000c} also reproduces the numerical halo abundances.

In order to assess the impact of the modeling of the mass function on the cosmological parameter inference from sparsity measurements, we extend the synthetic data analysis presented in Section 2.4. In particular, using the synthetic data set generated by solving Equation (4) with the ST-RayGal mass function, we perform a likelihood analysis assuming the ST-Despali mass function.

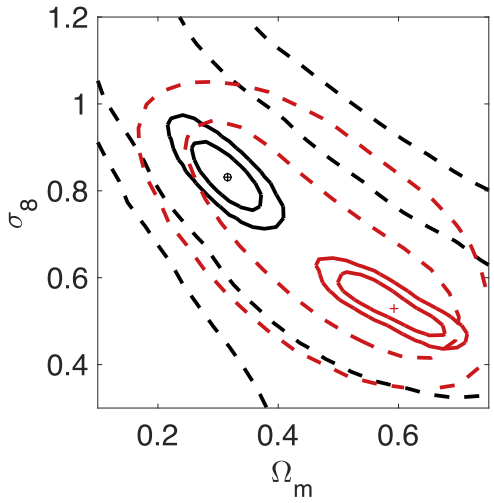


Figure 6. 1σ and 2σ credibility contours in the Ω_m–σ_8 plane from the likelihood analysis of average sparsity data with 1% (solid lines) and 20% (dashed lines) statistical errors generated by solving Equation (4) with the ST-RayGal mass function. The black lines correspond to the constraints shown in Figure 5 inferred assuming the ST-RayGal mass function. The constraints obtained assuming the ST-Despali mass function are shown as red lines. The black circle indicates the fiducial model parameters, while the plus signs indicate the best-fit parameter values for the different parameterizations.

In Figure 6 we plot the 1σ and 2σ credibility contours in the Ω_m–σ_8 plane assuming 1% and 20% statistical errors on the synthetic sparsity data, respectively. For comparison we also plot the contours shown in Figure 5 obtained by assuming the ST-RaGal mass function. We can clearly see that assuming the ST-Despali mass function when the synthetic data have been generated with the ST-RayGal mass function results in a systematic offset of the best-fit parameters. This bias is well above the statistical errors for sparsity measurements with 1% statistical uncertainties. We can also notice that the contours differ according to the assumed mass function. This is not surprising given the fact that the mass function parameterizations have been calibrated to simulations of different volume and mass resolution and encode differently the dependence on the cosmological parameters.

As already mentioned, the RayGalGroupSims simulation with a $(2.625\ \mathrm{Gpc}\ h^{-1})^3$ volume and a mass resolution of $m_p = 1.88 \cdot 10^{10}\ M_\odot h^{-1}$ provides a better sampling of the high mass-end of the halo mass function than the simulation ensemble used for the calibration of the ST-Despali mass function. As an example, the largest volume simulation from the SBARBINE suite presented in Despali et al. (2016) consists of a $(2\ \mathrm{Gpc}\ h^{-1})^3$ box with mass resolution $m_p = 6.35 \cdot 10^{11}\ M_\odot h^{-1}$. This impacts the accuracy of the mass function calibration, a point that can also be inferred by comparing the amplitude of the logarithmic differences of the calibrated formulae to the numerical estimations. As shown in Figure 14, the ST-RayGal parameterization reproduces the RayGalGroupSims mass function well within 5% across the entire mass range probed by the simulation and in the redshift interval $0 \leqslant z \leqslant 2$. In contrast, the ST-Despali parameterization shows differences with respect to the N-body results that at the high mass-end exceed the 5% level in the same redshift interval (see, e.g., Figure 11 in Despali et al. 2016). Conversely, the SBARBINE suite includes simulation runs with cosmological parameter values sufficiently far from the concordance ΛCDM model to better probe the cosmological dependence of the mass function on Ω_m and σ_8 than the ST-RayGal case. Therefore, this suggests that a simulation suite consisting of runs with volume and mass resolution similar to those of the RayGalGroupSims simulation for very different cosmological parameter values should provide a mass function parameterization sufficiently accurate to guarantee unbiased sparsity analyses in the case of sparsity data with errors at the ∼1% statistical level.

3.2. Hydrostatic Mass Estimates

Numerical simulation studies (see, e.g., Nagai et al. 2007; Meneghetti et al. 2010; Rasia et al. 2012; Velliscig et al. 2014; Biffi et al. 2016), as well as the analyses of observed cluster samples (Sereno & Ettori 2015), have shown that X-ray cluster masses obtained by solving the hydrostatic equilibrium (HE) equation are systematically underestimated compared to the true mass of the clusters.

The halo sparsity is unaltered by a constant systematic mass bias, since it is a mass ratio. In contrast, a radial-dependent shift affecting HE masses can alter the sparsity[10] and introduce a systematic error in the cosmological parameter inference. In addition to a bias effect, HE masses suffer from an intrinsic scatter of the order of 10%–20% (Rasia et al. 2012; Sereno & Ettori 2015). However, most of the sources of scatter act similarly over different radial ranges, so that this would induce negligible effects on sparsity.

The overall amplitude of the radial-dependent mass bias has been estimated in several numerical simulation studies. Nevertheless, the results differ as a consequence of the different numerical schemes used in the realization of the simulations, as well as the modeling and the implementation of the astrophysical processes that shape the properties of the gas in clusters. As an example, Rasia et al. (2012) have realized zoom simulations of 20 clusters at $z = 0.2$ with $M_{200c} > 4 \cdot 10^{14}\ M_\odot h^{-1}$ and found a 33% median mass bias at r_{500c} and 27.5% at r_{1000c} (see Table 2 in Rasia et al. 2012). These induce a relative shift with respect to the true average sparsity of ∼8%. A smaller amplitude of the mass bias has been found by Nagai et al. (2007); nevertheless, both these studies have neglected the impact of active galactic nuclei (AGNs) on the halo mass.

The OverWhelmingly Large Simulations project (Schaye et al. 2010) has performed a comprehensive study of the impact of baryonic feedback processes such as star formation, metal-line cooling, stellar winds, supernovae, and AGNs on the properties of galaxy clusters. Quite remarkably, these simulations reproduce the optical and X-ray observed features of groups and clusters of galaxies (McCarthy et al. 2010; Le Brun et al. 2014). The effects induced on the halo mass have been studied in detail in Velliscig et al. (2014). In this study, the authors have evaluated the median fractional mass bias y_Δ at $z = 0$ for $\Delta = 200c$, $500c$, and $2500c$ as a function of the halo DM mass. Their results have shown that baryonic effects can alter the total halo mass at the ∼15%–20% level for halos with $M_{200c} \sim 10^{13}\, M_\odot\ h^{-1}$ down to a few percent for the most

[10] Let M^t_Δ be the true halo mass and M^e_Δ be the estimated one at overdensity Δ. We define the fraction mass bias as $y_\Delta \equiv (M^e_\Delta - M^t_\Delta)/M^t_\Delta$. Then, the relative variation of the halo sparsity compared to its true value is given by

$$r_{\Delta_1,\Delta_2} \equiv \frac{\Delta s_{\Delta_1,\Delta_2}}{s_{\Delta_1,\Delta_2}} = \frac{1+y_{\Delta_1}}{1+y_{\Delta_2}} - 1, \quad (6)$$

from which it is evident that if the mass bias is independent of the cluster radius, $y_{\Delta_1} = y_{\Delta_2}$ and $\Delta s_{\Delta_1,\Delta_2} = 0$.

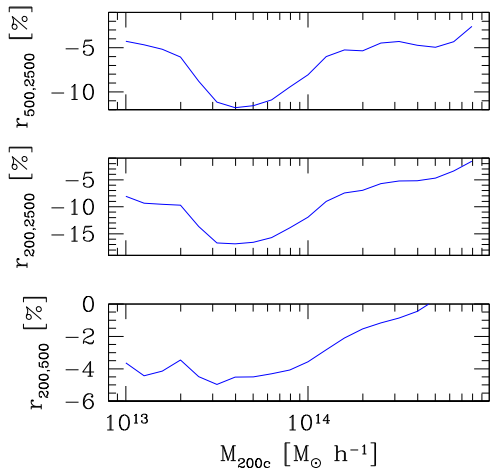


Figure 7. Percentage variation of the median halo sparsity $s_{200,500}$ (bottom panel), $s_{200,2500}$ (middle panel), and $s_{500,2500}$ (top panel) due to the radial mass bias induced by baryonic feedback processes as in the AGN 8.0 model investigated in Velliscig et al. (2014).

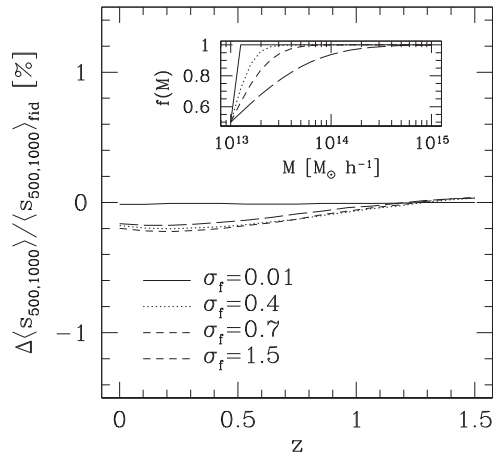


Figure 8. Relative difference of the average sparsity with respect to the case with no selection function for the *Planck* fiducial cosmology and different values of the selection function parameter $\sigma_f = 0.01$, 0.4, 0.7, and 1.5. The inset plot shows the form of the selection function for the different values of σ_f.

massive systems with $M_{200c} \sim 10^{15}\,M_\odot\ h^{-1}$. We use their results for the feedback model AGN 8.0 (see Figure 2 in Velliscig et al. 2014) reproducing the observed X-ray profile of clusters (Le Brun et al. 2014). In Figure 7 we plot the percentage variation of the median halo sparsity for $s_{200,500}$ (bottom panel), $s_{200,2500}$ (middle panel), and $s_{500,2500}$ (top panel) as given by Equation (6). We can see that at large radii the effect of baryonic feedback causes the sparsity to be underestimated by $\Delta\langle s_{200,500}\rangle/\langle s_{200,500}\rangle \lesssim 4\%$. For inner radii the effect is larger, but limited to $\lesssim$15% for $s_{200,2500}$ and $\lesssim$10% for $s_{500,2500}$. In any case, we notice that for massive systems with $M_{200c} \gtrsim 10^{14}\,M_\odot\ h^{-1}$ the level of bias on the sparsity is below ∼5%.

The study presented in Velliscig et al. (2014) has focused on how baryonic processes alter halo masses. On the other hand, in our analysis we are particularly interested in the effects on the HE estimated masses. This has been recently investigated by Biffi et al. (2016), who have performed zoom simulations of 29 clusters at $z = 0$ with masses $M_{200c} \gtrsim 10^{14}\,M_\odot\ h^{-1}$. These simulations account for metallicity-dependent radiative cooling, time-dependent UV background, star formation, metal enrichment, stellar winds, and AGN feedback. The authors have estimated the fractional median hydrostatic mass bias for cool-core (CC), non-CC, regular, and disturbed systems for overdensity thresholds $\Delta = 200c$, $500c$, and $2500c$ (see Table 1 in Biffi et al. 2016). Using these results, we linearly extrapolate the hydrostatic mass bias at $\Delta = 1000c$ and compute the fraction bias on the sparsity $s_{500,1000}$, which we report in Table 1 for different cluster categories. We can see that the hydrostatic mass bias induces a shift on the true cluster sparsity of 0.1%–0.3% (non-CC and regular) and 2%–4% (CC and disturbed), which is largely in agreement with the estimates we have obtained using the results from Velliscig et al. (2014).

Further numerical analyses are nonetheless necessary since no study has so far investigated in detail how the hydrostatic mass bias evolves with time and therefore how the bias on the sparsity evolves with redshift. Velliscig et al. (2014) have shown that the baryonic effects that alter M_{200c} at $z = 0$ tend to be smaller (by ∼5%) at $z = 1$. If such a trend holds for larger overdensity thresholds, that would imply that the bias on the halo sparsity is a decreasing function of redshift.

Table 1
Relative Variation of the Sparsity $s_{500,1000}$ due to Hydrostatic Mass Bias for CC, NCC, Regular, and Disturbed Clusters Simulated in Biffi et al. (2016)

Cluster State	$r_{500,1000}$ (%)
CC	−3.7
NCC	0.1
Regular	0.3
Disturbed	−2.0

Overall, all these elements confirm the strength of the cluster sparsity against possible mass bias systematics. The advantage is twofold. In fact, being a mass ratio, any systematic error affecting cluster mass estimates is suppressed. Moreover, one can focus on the sparsity at overdensity thresholds corresponding to external regions of the cluster mass profile where baryonic effects are subdominant. It is also worth noticing that though hydrostatic masses depend on the choice of a fiducial cosmology through the angular diameter distance, the sparsity, being a mass ratio, is independent of such an assumption.

3.3. Selection Effects

A final remark concerns selection effects. In principle, we do not expect a significant contribution since we have seen that average sparsity as predicted by Equation (4) is largely independent of the lower limit of integration. To have a quantitative estimate of potential systematics induced by the shape of the selection function, we multiply the integrands on both sides of Equation (4) by a selection function of the form

$$f(M_\Delta) = \frac{1}{2}\left[1 + \mathrm{erf}\left(\frac{\ln M_\Delta - \ln M_\Delta^{\min}}{\sqrt{2}\,\sigma_f}\right)\right], \qquad (7)$$

where σ_f modulates the shape of the selection function.

In Figure 8 we plot the relative difference of the redshift evolution of the average sparsity with respect to the case $f(M_\Delta) = 1$ for the fiducial *Planck* cosmology and for different values of $\sigma_f = 0.01$, 0.4, 0.7, and 1.5. We can see that the differences are at the subpercent level.

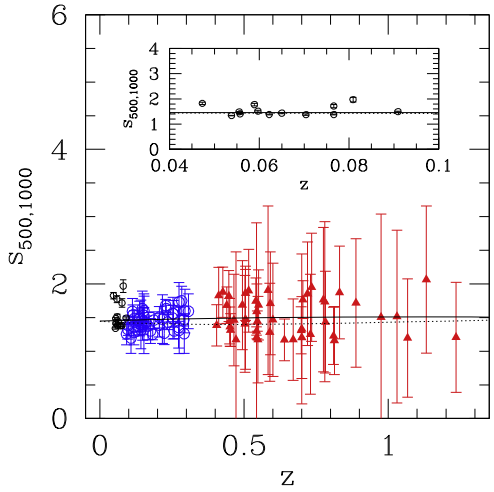


Figure 9. Sparsity of X-ray clusters. The low-redshift sample consists of clusters with mass measurements from Ettori et al. (2017), S. Ettori et al. (2017, in preparation), and V. Ghirardini et al. (2017, in preparation), also shown in the inset plot (black open circles), and Ettori et al. (2010) (blue open circles). The high-redshift sample consists of clusters with mass estimates from Amodeo et al. (2016; red filled triangles). The black solid line and the black dotted line correspond to the best-fit ΛCDM models inferred assuming the ST-RayGal and ST-Despali mass functions, respectively. We may notice four clusters at $z < 0.1$ whose sparsity significantly departs from the best fit. We have checked that excluding these outliers from the analysis does not alter the result of the cosmological parameter inference.

4. Sparsity of X-Ray Clusters and Cosmological Parameter Constraints

We estimate the halo sparsity of a set of X-ray galaxy clusters with hydrostatic mass measurements. The data set consists of a low-redshift sample of 57 clusters ($0.05 < z < 0.3$) from Ettori et al. (2010, 2017), S. Ettori et al. (2017, in preparation), and V. Ghirardini et al. (2017, in preparation) and a high-redshift sample of 47 clusters ($0.4 < z < 1.2$) presented in Amodeo et al. (2016). DM masses M_{500c} and M_{1000c} have been estimated by solving the HE equation (see, e.g., Sarazin 1986; Ettori 2013). We compute the sparsity of each cluster in the catalogs, $\hat{s}_{500,1000} = M_{500c}/M_{1000c}$, and estimate the uncertainty by propagating the mass measurement errors. These are shown in Figure 9.

For simplicity we have neglected mass correlation effects: these may be present as a result of the mass measurement methodology that assumes a functional form of the DM halo profile.[11] Systematics affecting the HE mass estimate can be more important. In the case of the high-redshift sample, Amodeo et al. (2016) have tested the consistency of the HE masses for a subset of 32 clusters for which gravitational lensing measurements were available in the literature (LC^2-`single` catalog from Sereno 2015). They have found a good agreement within the large statistical uncertainties with $\ln(M_{\rm HE}/M_{\rm lens}) = 0.16 \pm 0.65$. For the low-redshift sample there is no available comparison; however, we noticed that the data set from Ettori et al. (2010) consists of massive clusters for which mass measurement errors are larger than the expected bias from baryonic feedback discussed in Section 3.2. In the case of the very low redshift sample by Ettori et al. (2017), S. Ettori et al. (2017, in preparation), and V. Ghirardini et al. (2017, in preparation), HE mass uncertainties are at the few percent level, and we cannot a priori exclude that some of the sparsity measurements are affected by radial mass bias. After all, we can see in Figure 9 that the sparsity of four of the clusters in the very low redshift sample significantly deviates from the values of the other objects in the data set. We have found that removing these objects from the data analysis leaves the cosmological results unaltered. As seen in Section 2.3, this is a direct consequence of the fact that the cosmological signal is largest at $z \sim 0.5$. Nevertheless, to test the stability of the cosmological analysis against possible contamination from HE mass bias, we perform an additional analysis assuming a systematic redshift-dependent shift of the measured cluster sparsity. More specifically, we assume a 5% shift of the cluster sparsity at $z = 0$ linearly reducing to 2% at $z = 1$. This is an extremely conservative bias model, especially if compared to the level of bias discussed in Section 3.2. In fact, it implies that the HE mass determination of each cluster systematically underestimates M_{500c} by 28% and M_{1000c} by 35% at $z = 0$, and by 23% and 30%, respectively, at $z = 1$ (consistently with the 5% reduction found for M_{200c} estimates in Velliscig et al. 2014).

Since we compare individual cluster sparsity estimates to the predictions of the ensemble average sparsity, we account for the intrinsic dispersion of the halo sparsity discussed in Section 2.2 by adding in quadrature a conservative and absolute 0.2 intrinsic scatter (consistent with N-body simulation results shown in the inset plot of Figure 2) to the statistical error.

We perform a Markov chain Monte Carlo data analysis to derive constraints on the ΛCDM model parameters, (Ω_m, σ_8, h, n_s, $\Omega_b h^2$). To reduce the effect of parameter degeneracies, we assume a set of Gaussian priors on $n_s \sim \mathcal{N}(0.963, 009)$ consistently with *Planck* results (Planck Collaboration et al. 2016a), $h \sim \mathcal{N}(0.688, 0.033)$ from Efstathiou (2014), and $\Omega_b h^2 \sim \mathcal{N}(0.022, 0.002)$ consistent with big bang nucleosynthesis bounds (Cyburt et al. 2016). We assume flat priors for $\Omega_m \sim \mathcal{U}(0.05, 0.95)$ and $\sigma_8 \sim \mathcal{U}(0.2, 1.8)$. In order to evaluate the impact of the prior on h, we have also performed a likelihood analysis of the full cluster sample assuming a Gaussian *HST* prior $h \sim \mathcal{N}(0.732, 0.024)$ from Riess et al. (2016).

We evaluate the following χ^2:

$$\chi^2 = \sum_i \frac{[\hat{s}^i_{500,1000} - \langle s^{\rm th}_{500,1000}(z_i)\rangle]^2}{\sigma^2_{\rm int} + \sigma^2_{s^i_{500,1000}}}, \quad (8)$$

where $\hat{s}^i_{500,1000}$ is the sparsity of the ith cluster in the catalog, $\langle s^{\rm th}_{500,1000}(z_i)\rangle$ is the theoretical model prediction given by Equation (4) assuming a given mass function model, $\sigma_{\rm int} = 0.2$ is the intrinsic scatter of the halo sparsity[12] (conservatively set to a value consistent with the N-body results), and $\sigma_{s^i_{500,1000}}$ is the error on the cluster sparsity measurement.

We use the Metropolis–Hastings algorithm to generate 15 independent random chains of 2×10^5 samples and evaluate the rejection rate every 100 steps and adjust the width of the parameters dynamically. We check the convergence of the chains using the Gelman–Rubin test (Gelman & Rubin 1992).

[11] Given that the sparsity is a mass ratio, a positive correlation r between the estimates of M_{500c} and M_{1000c} would imply that we are overestimating the sparsity errors by a factor of $\sim 1/\sqrt{(1-r)}$. For instance, if $r \sim 0.5$, as is reasonable to expect, this would correspond to a 30% overestimation and thus result in more conservative constraints on the cosmological parameters.

[12] In principle, one can attempt to infer the intrinsic scatter from the data regression with the other cosmological parameters.

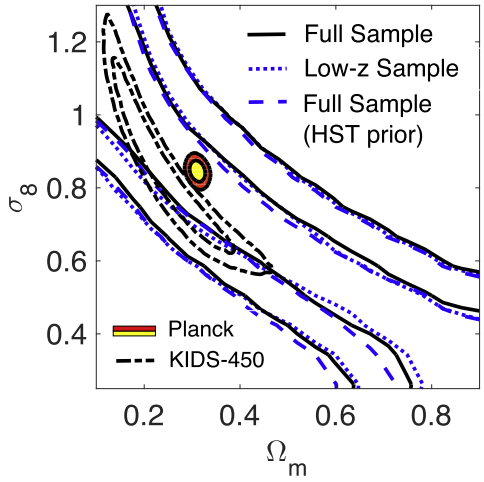


Figure 10. Marginalized 1σ and 2σ contours in the Ω_m–σ_8 plane assuming the ST-RayGal mass function using the full X-ray cluster data set (black solid lines), the low-z redshift sample only (blue dotted lines), and the case of the *HST* prior on h (blue dashed lines). For comparison we also plot the contours from the *Planck* cosmological data analysis (Planck Collaboration et al. 2016a) and KIDS-450 (Hildebrandt et al. 2017).

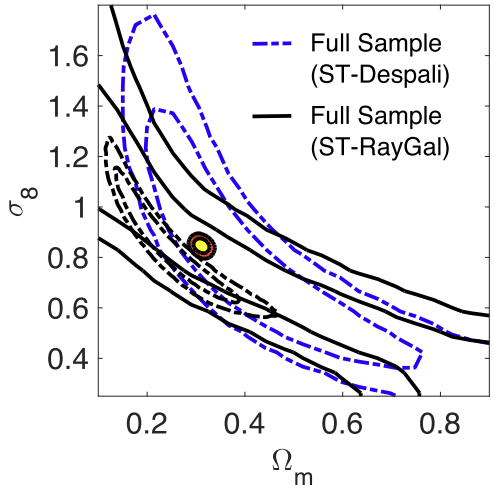


Figure 11. Marginalized 1σ and 2σ contours in the Ω_m–σ_8 plane as in Figure 10. Here, the blue dashed lines are the contours inferred assuming the ST-Despali mass function.

The results of the likelihood data analysis assuming the ST-RayGal mass function are summarized in Figure 10, where we plot the marginalized 1σ and 2σ credibility contours in the Ω_m–σ_8 plane for the different cases. For comparison we also plot the marginalized credibility contours from the *Planck* cosmological data analysis (Planck Collaboration et al. 2016a) and the weak gravitational lensing from KIDS-450 (Hildebrandt et al. 2017). We can see that the constraints on Ω_m and σ_8 are rather weak. Given the large uncertainties of the sparsity sample at $z \gtrsim 0.4$, this is not surprising since the variation of the sparsity with respect to σ_8 is the largest at $z \sim 0.4$, while that with respect to Ω_m remains quite flat for $z \gtrsim 0.5$ (see top panel in Figure 4). The best-fit model corresponds to $\Omega_m \simeq 0.4$ and $\sigma_8 \simeq 0.6$. We plot the associated average sparsity as a function of redshift as a black solid line in Figure 9. Notice the strong degeneracy between Ω_m and σ_8. As discussed in Section 2.3, this is expected given the sensitivity of the halo sparsity to $S_8 \equiv \sigma_8\sqrt{\Omega_m}$, for which we find $S_8 = 0.40 \pm 0.11$ at 1σ.

As we can see in Figure 10, the credibility contours do not significantly differ from those inferred under the *HST* prior. This is also consistent with the analysis presented in Section 2.3, which indicates that the halo sparsity is less sensitive to h than σ_8, Ω_m, and n_s. Indeed, changing the priors on n_s can have a more significant impact on the inferred constraints. However, n_s is tightly constrained by the *Planck* data, while there are larger uncertainties on the value of h, which is why we have tested the sensitivity of the constraints to the h prior.

In Figure 10 we also plot the credibility contours inferred using the low-z sample ($z \lesssim 0.4$) only. These do not differ from those obtained using the full sample, which is not surprising given the larger uncertainties of the high-z sample. Overall, the inferred credibility contours overlap with those inferred from *Planck* within 1σ, as well as those from the KIDS-450 data set.

In Figure 11 we plot the constraints in the Ω_m–σ_8 plane inferred assuming the ST-Despali mass function. Differently from the ST-RayGal case, we find bounded contours at 1σ, though still spread over a larger portion of the parameter space. The one-dimensional marginalized constraints are $\Omega_m = 0.42 \pm 0.17$ and $\sigma_8 = 0.80 \pm 0.31$ at 1σ, with the best-fit values being $\Omega_m = 0.36$ and $\sigma_8 = 0.74$. We plot the associated average sparsity as a function of redshift as a black dotted line in Figure 9. From the analysis of the Monte Carlo chains we obtain $S_8 = 0.48 \pm 11$ at 1σ, which is consistent with the constraints found using the ST-RayGal mass function. As we can see in Figure 11, the contours are statistically consistent with those inferred from the ST-RayGal analysis, though deviations are noticeable in the tail of the distribution for low values of Ω_m and large values of σ_8. This is not unexpected since in this range of the parameter space the mass function calibration may deviate from that of the vanilla ΛCDM model of the RayGalGroupSims simulation. The bounds are compatible with the *Planck* results and consistent with those from the KIDS-450 analysis.[13]

We have limited the analysis including the systematic HE mass bias model discussed at the beginning of this section to the case of the ST-Despali mass function. The results of the likelihood data analysis give $S_8 = 0.51 \pm 0.11$, which is consistent with the results obtained assuming no systematic bias model.

5. X-Ray Cluster Sparsity Forecasts

Future observational programs will provide increasingly large samples of clusters. Surveys such as *eROSITA* (Merloni et al. 2012) are expected to detect several hundred thousands of clusters across a large redshift range. Cosmological parameter constraints will be inferred from accurate measurements of cluster number counts and spatial clustering (see, e.g., Pillepich et al. 2012).

Sparsity measurements capable of providing constraints that are competitive with respect to those inferred from other cosmological probes strongly depend on the availability of accurate mass estimations. In the case of large data sets, such as

[13] Several large-scale structure data analyses have constrained combinations of Ω_m and σ_8. As an example, SZ cluster abundance data from the South Pole Telescope (SPT) survey give $\sigma_8\,(\Omega_m/0.27)^{0.3} = 0.797 \pm 0.031$ (de Haan et al. 2016). The analysis of the cluster sparsity presented here gives consistent bounds, $\sigma_8(\Omega_m/0.27)^{0.3} = 0.87 \pm 0.26$. Similarly, measurements of the galaxy clustering from the Dark Energy Survey (DES) constrain $\sigma_8(\Omega_m/0.3)^{0.16} = 0.74 \pm 0.12$ (Kwan et al. 2017), and we find again a result consistent within 1σ, $\sigma_8(\Omega_m/0.3)^{0.16} = 0.83 \pm 0.29$.

those from *eROSITA*, cluster masses will be measured through the use of observationally calibrated scaling relations (see, e.g., Maughan et al. 2012; Ettori 2013, 2015). More precise estimates, for instance, using HE masses, require observations that are able to resolve the cluster mass profile. However, these may be available only for smaller cluster samples through follow-up observations.

Here we perform a Fisher matrix forecast of the cosmological parameter errors from sparsity measurements to determine the type of galaxy cluster observations needed to derive competitive constraints with respect to those that can be obtained with other standard probes such as the CMB.

To this purpose we evaluate the Fisher matrix:

$$F_{\mu\nu} = \sum_i \frac{1}{\sigma_{z_i}^2} \frac{\partial \langle s_{500,1000}(z_i)\rangle}{\partial\theta_\mu} \frac{\partial \langle s_{500,1000}(z_i)\rangle}{\partial\theta_\nu}\Bigg|_{\hat{\theta}_\mu}, \quad (9)$$

where $\theta_\mu = (\Omega_m, \sigma_8, h, n_s, \Omega_b)$ are the cosmological parameters, $\hat{\theta}_\mu$ is the fiducial parameter value, and σ_{z_i} is the statistical error on the mean sparsity. We compute the partial derivatives in Equation (9) using a five-point stencil approximation. We model the error on the average sparsity as

$$\sigma_{z_i} = \langle s^{\rm fid}_{500,1000}(z_i)\rangle \, e_M \sqrt{\frac{2}{N(z_i)}}, \quad (10)$$

where $\langle s^{\rm fid}_{500,1000}(z_i)\rangle$ is the fiducial sparsity value, e_M is the fraction error on mass measurements, and $N(z_i)$ is the number of clusters at redshift z_i, given by

$$N(z_i) \equiv A_{\rm survey}\, \Delta z\, f\, \frac{dN}{dzdA}(z_i), \quad (11)$$

where $A_{\rm survey}$ is the survey area, Δz is the size of the redshift bins, f is the fraction of clusters with mass measurement error e_M, and $(dN/dzdA)(z)$ is the cluster number count distribution. Again, for simplicity we neglect correlations in the estimation of the masses M_{500c} and M_{1000c}. Notice that, as in the case of the synthetic likelihood test presented in Section 4, we do not add in quadrature the intrinsic scatter of the halo sparsity to the statistical error as in the data analysis described in Section 4. This is because, in the spirit of the Fisher matrix calculation, we compare predictions of the ensemble average sparsity not to the sparsity of an individual cluster at a given redshift, but rather to the estimated average sparsity from an ensemble of $N(z_i)$ clusters.

We assume a *Planck* fiducial ΛCDM cosmology and consider a full-sky survey with cluster number count distribution consistent with an *eROSITA*-like survey. This is expected to detect $\sim 10^5$ clusters with mass $\gtrsim 10^{13}\, h^{-1}\, M_\odot$. To this purpose we estimate the cluster number counts as a function of redshift for our fiducial cosmology by integrating the ST-RayGal mass function with M_{500c} and imposing a flux cut $F_{\rm X,cut} = 4.3 \times 10^{-14}$ erg s^{-1} cm^{-2}, where we have used the luminosity–mass relation from Mantz et al. (2010) with no intrinsic scatter. The predicted number count distribution is shown in Figure 12. We may notice that this is consistent with the redshift distribution estimated by Pillepich et al. (2012; see their Figure 3 for the photon count rate threshold corresponding to $M^{\rm cut}_{500c} \gtrsim 5 \times 10^{13}\, h^{-1}\, M_\odot$), with a total count of $\sim 3 \times 10^4$ clusters. For simplicity, here we only consider redshift bins of size $\Delta z = 0.1$ in the redshift range $0 \lesssim z \lesssim 1.4$.

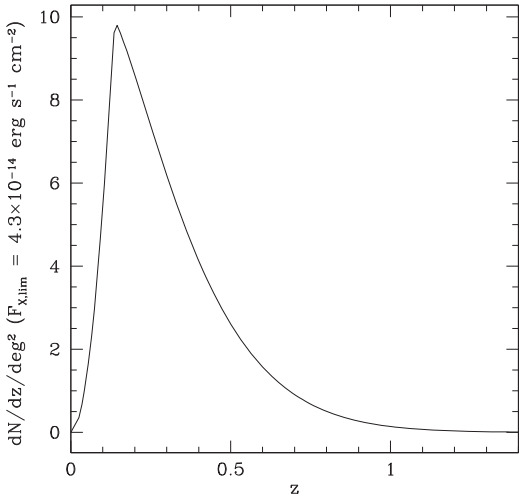


Figure 12. Expected redshift distribution of clusters of an *eROSITA*-like survey with X-ray flux cut $F_{\rm X,cut} = 4.3 \times 10^{-14}$ erg s^{-1} cm^{-2} for our fiducial cosmological model.

Table 2
Marginalized Errors on Cosmological Parameters from the Fisher Matrix Analysis of *Small-sample, High-precision* Sparsity Measurements in Combination with *Planck* Constraints

	Planck Only	$+\langle s_{500,1000}(z)\rangle$ ($e_M = 0.01, f = 0.01$)	$+\langle s_{500,1000}(z)\rangle$ ($e_M = 0.05, f = 0.1$)
σ_{Ω_m}	0.01082	0.01022/0.00571	0.01035/0.00684
σ_{σ_8}	0.01396	0.00597/0.00780	0.00720/0.00926
σ_{n_s}	0.00428	0.00414/0.00300	0.00418/0.00328
σ_h	0.00763	0.00723/0.00411	0.00732/0.00490
σ_{Ω_b}	0.00095	0.00090/0.00053	0.00091/0.00062

Note. The numbers quoted on the left (right) correspond to the Fisher forecast based on the ST-RayGal (ST-Despali) mass function.

We limit our analysis to two different observational scenarios: *small-sample, high-precision* sparsity measurements with mass errors of $e_M = 0.01$ for ∼300 clusters ($f = 0.01$) and $e_M = 0.05$ for ∼3000 clusters ($f = 0.10$), and *large-sample, low-precision* sparsity measurements with mass errors of $e_M = 0.1$ for ∼6000 clusters ($f = 0.2$) and $e_M = 0.2$ for all clusters ($f = 1$). The latter scenario considers the possibility of measuring masses over a large sample of clusters through well-calibrated scaling relations whose validity should be limited to the ∼10%–30% level.

We combine the Fisher matrix from Equation (9) to the Planck–Fisher matrix, which has been computed using the code CosmoFish (Raveri et al. 2016a, 2016b).

The results are summarized in Tables 2 and 3. In all cases we can see that including the information from the halo sparsity improves the CMB constraints from *Planck*. Indeed, the level of improvement depends on the observational configuration considered. Quite remarkably, we find that a 1% mass error estimation for a sample of ∼300 clusters has the greatest impact in reducing the *Planck* errors on several parameters. For instance, we find an improvement of a factor of ∼2.3 on the estimation of σ_{σ_8} in the ST-RayGal case, while assuming the ST-Despali mass function we find an improvement of a factor

Table 3
As in Table 2, but for *Large-sample, Low-precision* Sparsity Measurements

	Planck Only	$+\langle s_{500,1000}(z)\rangle$ ($e_M = 0.10, f = 0.2$)	$+\langle s_{500,1000}(z)\rangle$ ($e_M = 0.20, f = 1$)
σ_{Ω_m}	0.01082	0.01044/0.00751	0.01041/0.00731
σ_{σ_8}	0.01396	0.00850/0.01010	0.00805/0.00984
σ_{n_s}	0.00428	0.00420/0.00345	0.00419/0.00340
σ_h	0.00763	0.00738/0.00536	0.00736/0.00522
σ_{Ω_b}	0.00095	0.00092/0.00068	0.00092/0.00066

of $\sim$1.9 on σ_{Ω_m} and $\sim$1.8 on σ_{σ_8}. Even for the realistic scenario with 20% mass errors, we find up to $\sim$30% improvement of the *Planck* constraints. Again, assuming the ST-Despali mass function systematically predicts smaller parameter errors than those obtained with the ST-RayGal mass function.

Compared to other cosmic probes, such as the combination of CMB constraints with those from cluster number counts and angular clustering studied in Pillepich et al. (2012), we find that the sparsity can provide cosmological parameter constraints of the same order (see, e.g., Table B2 in Pillepich et al. 2012).

6. Conclusions

In this work we have presented a first cosmological analysis of the DM halo sparsity. This characterizes halos in terms of the ratio of halo masses at two different overdensities and carries cosmological information encoded in the mass profile of halos that can be retrieved from mass measurements of galaxy clusters.

Building on the work of Balmes et al. (2014), we have tested the sparsity properties using halo catalogs from a large-volume, high-resolution *N*-body simulation. In particular, we have shown that the average sparsity of an ensemble of halos can be accurately predicted from prior knowledge of the halo mass function. To this purpose we have introduced the ST-RayGal parameterization, which reproduces to great accuracy the numerical halo mass function for halo masses M_{200c}, M_{500c}, and M_{1000c} and allows us to recover the measured average sparsity values at different redshift snapshots to the subpercent level.

We have tested the accuracy of the theoretical predictions assuming other mass function parameterizations proposed in the literature. Depending on the mass function model, we found deviations with respect to the average sparsity from the *N*-body halo catalogs up to the 10% level.

The possibility of predicting the average sparsity for a given set of cosmological parameters enables us to perform a cosmological model parameter inference using cluster sparsity measurements. To test this, we have generated a synthetic set of data and performed a likelihood analysis, from which we have retrieved the input fiducial cosmology.

Systematic errors affecting halo sparsity data analyses may arise primarily from uncertainties in the theoretical modeling of the halo mass function and the radial-dependent cluster mass bias from baryonic feedback processes. Here we have performed an analysis of these systematics. Quite importantly, using results from state-of-art numerical simulations, we show that for massive systems baryonic effects alter the halo sparsity at the few percent level. This is subdominant compared to the uncertainties from mass estimation errors of currently available cluster data sets. We find that cluster selection effects have a negligible impact on sparsity, which is an obvious advantage compared to other cluster cosmological proxies, such as the number counts or the spatial clustering.

We have estimated the sparsity of a sample of X-ray clusters with hydrostatic mass measurements and performed a Markov chain Monte Carlo likelihood data analysis to infer constraints Ω_m and σ_8. We find weak marginalized bounds on Ω_m and σ_8. Assuming the mass function from Despali et al. (2016) gives the strongest bound, in particular, we find $\Omega_m = 0.42 \pm 0.17$ and $\sigma_8 = 0.80 \pm 0.31$ at 1σ, corresponding to $S_8 = 0.48 \pm 0.11$. In all cases the inferred constraints are compatible with those inferred from the *Planck* cosmological data analysis within 1σ. We find these results to be stable against a conservative systematic bias model accounting for baryonic effects on cluster mass estimates.

Future cluster surveys can provide larger sparsity data sets. Using a Fisher matrix approach, we have investigated their complementarity with respect to CMB observations from *Planck*. In particular, we have performed a parameter error forecast for different observational scenarios and found that sparsity measurements from a small cluster sample of $\sim$300 clusters with mass uncertainties of 1% can improve *Planck* constraints on Ω_m and σ_8 by approximately a factor of 2. However, this requires a control of systematic errors due to hydrostatic mass bias.

Cluster mass measurements from SZ and lensing observations may also provide viable data sets to estimate the halo sparsity, and we leave such studies to future works.

We would like to thank Matteo Martinelli for providing us with the Planck–Fisher matrix. P.S.C. is grateful to Joop Schaye for useful discussions. P.S.C., Y.R., and M.-A.B. are thankful to Fabrice Roy for technical support. S.E. and M.S. acknowledge the financial support from contracts ASI-INAF I/009/10/0, NARO15 ASI-INAF I/037/12/0, and ASI 2015-046-R.0. The research leading to these results has received funding from the European Research Council under the European Union Seventh Framework Programme (FP7/2007-2013 grant agreement no. 279954). We acknowledge support from the DIM ACAV of the Region Île-de-France. This work was granted access to the HPC resources of TGCC under allocation 2016-042287 made by GENCI (Grand Équipement National de Calcul Intensif).

Appendix
Halo Mass Function Parameterization

We use the numerical mass functions estimated from the RayGalGroupSims simulation SOD halo catalogs with mass M_{200c}, M_{500c}, and M_{1000c}, to calibrate at each redshift snapshot the coefficients of the ST mass function formula (Sheth & Tormen 1999):

$$\frac{dn}{dM} = \frac{\rho_m}{M}\left(-\frac{1}{\sigma}\frac{d\sigma}{dM}\right)A\frac{\delta_c}{\sigma}\sqrt{\frac{2a}{\pi}}\left[1+\left(a\frac{\delta_c^2}{\sigma^2}\right)^{-p}\right]e^{-\frac{a\delta_c^2}{2\sigma^2}}, \quad (12)$$

where ρ_m is the present mean matter density, δ_c is the linearly extrapolated spherical collapse threshold, which we compute using the formula from Kitayama & Suto (1996), and

$$\sigma^2(M, z) = \frac{1}{2\pi^2}\int dk\, k^2 P(k, z)\tilde{W}^2[k\, R(M)] \quad (13)$$

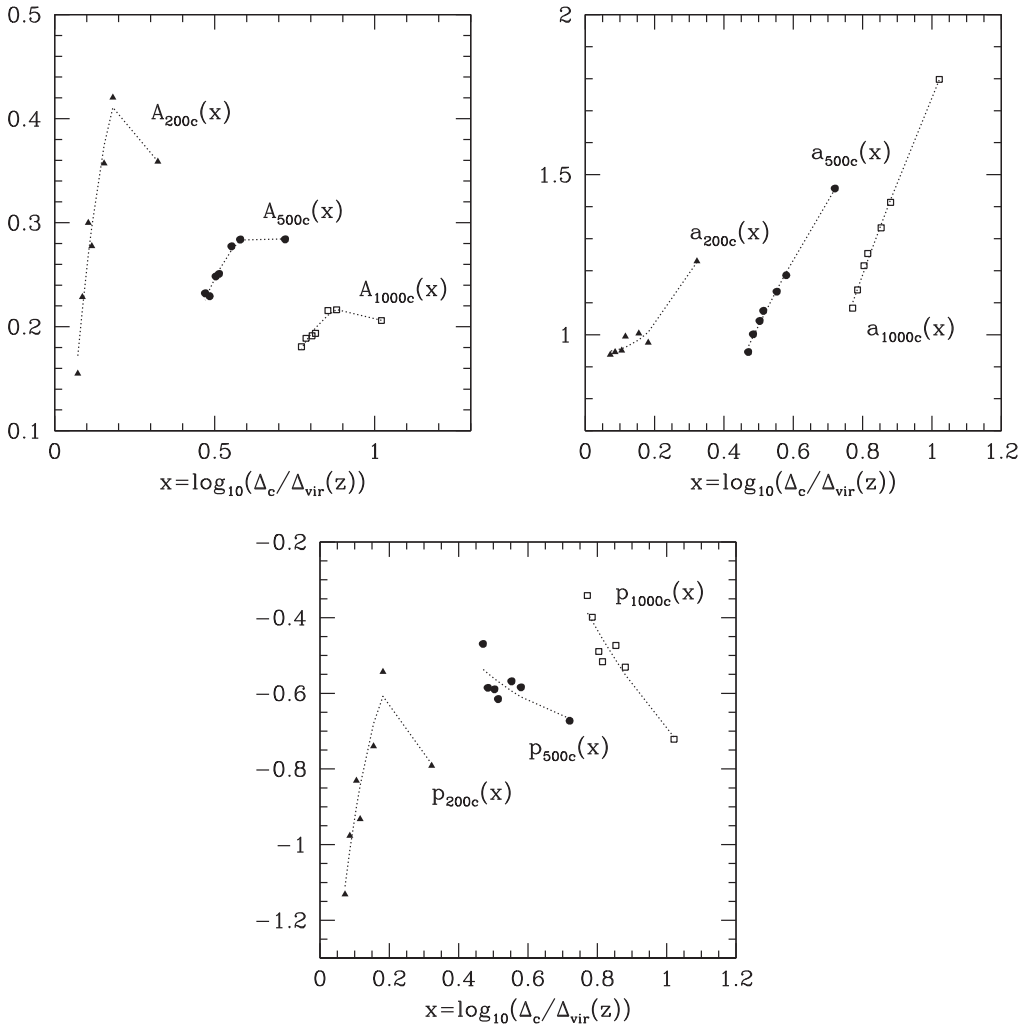


Figure 13. Comparison of the ST best-fit parameters' dependence on $x = \log_{10}(\Delta_c/\Delta_{\rm vir}(z))$ and the best-fit quadratic functions for A_{Δ_c} (top left panel), a_{Δ_c} (top right panel), and p_{Δ_c} (bottom panel) for $\Delta_c = 200$, 500, and 1000, respectively.

Table 4
Best-fit Coefficients of the ST Mass Function for Halos with Masses M_{200c}, M_{500c}, and M_{1000c}

z	A_{200c}	a_{200c}	p_{200c}	A_{500c}	a_{500c}	p_{500c}	A_{1000c}	a_{1000c}	p_{1000c}
0.00	0.35884	1.2300	−0.79142	0.28401	1.4568	−0.67260	0.20596	1.7978	−0.72148
0.50	0.42038	0.9752	−0.54330	0.28378	1.1859	−0.58425	0.21628	1.4134	−0.53098
0.66	0.35697	1.0039	−0.74000	0.27724	1.1347	−0.56833	0.21555	1.3339	−0.47343
1.00	0.27751	0.9944	−0.93238	0.25082	1.0470	−0.61536	0.19365	1.2537	−0.51639
1.14	0.29991	0.9505	−0.83109	0.24834	1.0429	−0.58941	0.19134	1.2156	−0.48951
1.50	0.22855	0.9457	−0.97637	0.22936	1.0014	−0.58554	0.18885	1.1400	−0.39898
2.00	0.15502	0.9375	−1.13120	0.23210	0.9459	−0.46949	0.18072	1.0830	−0.34148

is the variance of the linear density field smoothed on a spherical volume of radius R enclosing the mass $M = 4/3\pi\rho_m R^3$, with $P(k, z)$ being the linear matter power spectrum at redshift z and

$$\tilde{W}^2[k\,R(M)] = \frac{3}{(kR)^3}[\sin(kR) - (kR)\cos(kR)]. \qquad (14)$$

We determine the best-fit ST coefficients using a Levenberg–Marquardt minimization scheme. These are quoted in Table 4 for halo masses M_{200c}, M_{500c}, and M_{1000c}. We find the best-fit functions to have logarithmic deviations with respect to the numerical estimates to better than 5%.

In order to extrapolate the mass functions at any given redshift, we follow the approach of Despali et al. (2016) and

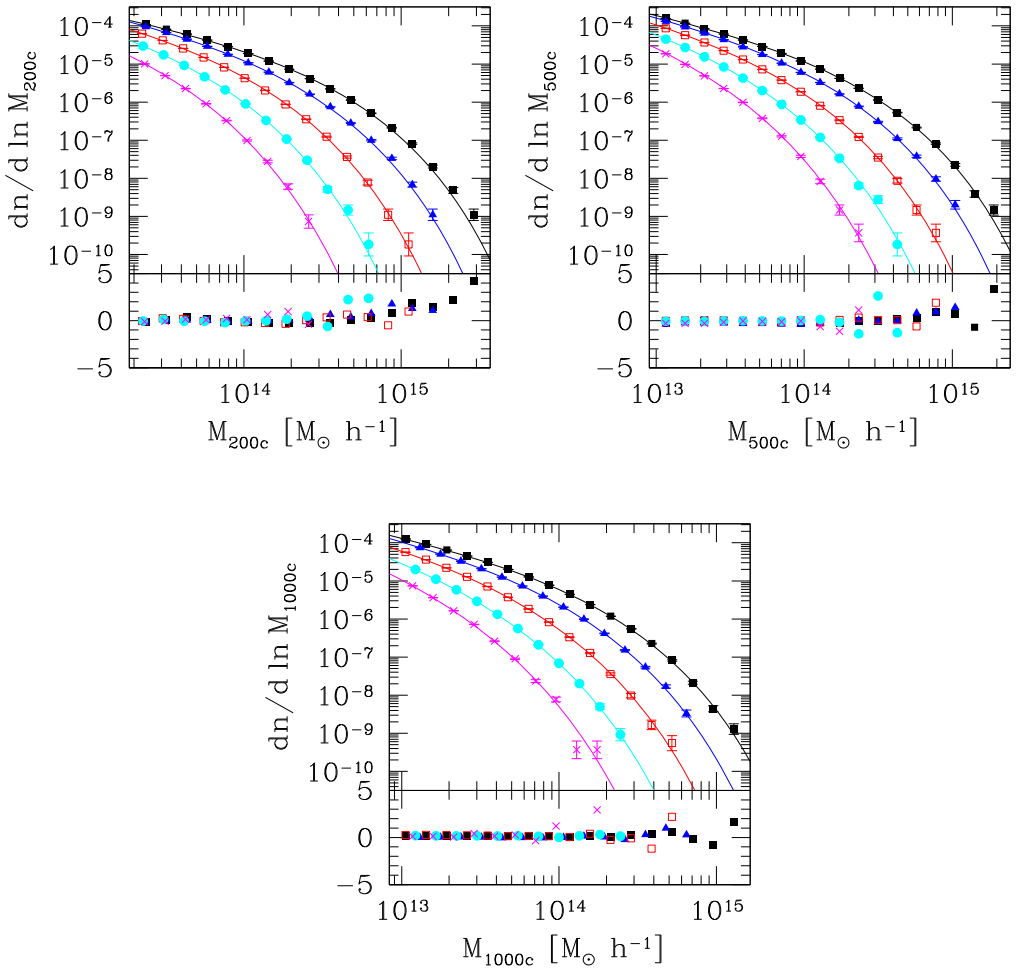


Figure 14. Halo mass function from the RayGalGroupSims simulation for SOD halos with mass M_{200c} (top left panel), M_{500c} (top right panel), and M_{1000c} (bottom panel) at $z = 0$, 0.5, 1, 1.5, and 2 (top to bottom). The solid lines are the ST-RayGal mass functions with coefficients given by Equations (15), (16), and (17). The logarithmic residual is shown in the bottom panel: as we can see, deviations are within the 5% level across the entire mass range.

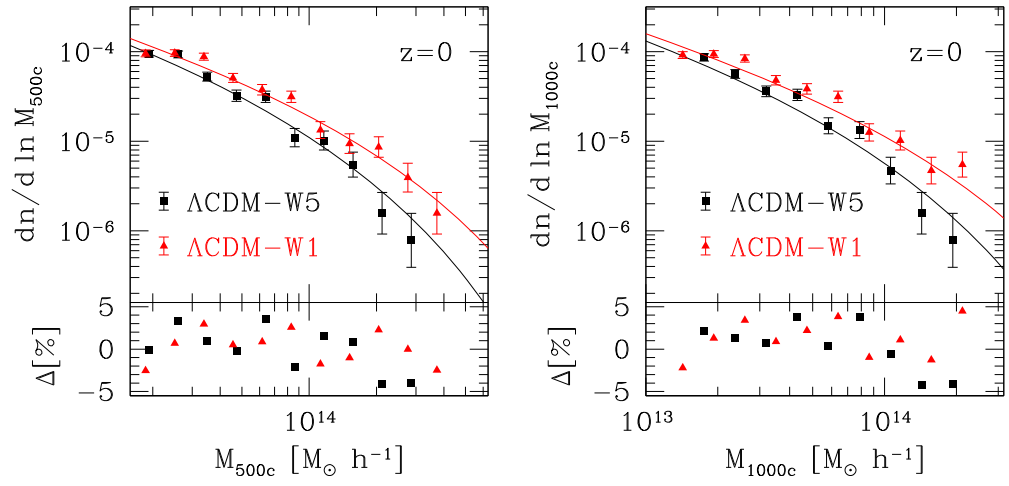


Figure 15. SOD halo mass functions from ΛCDM-W5 (black squares) and ΛCDM-W1 (red triangles) with mass M_{500c} (left panel) and M_{1000c} (right panel), respectively, against the ST-RayGal predictions.

parameterize the redshift dependence of the ST coefficients in terms of the variable $x = \log_{10}(\Delta/\Delta_{\rm vir}(z))$, where $\Delta_{\rm vir}(z)$ is the virial overdensity as given by the formula derived in Bryan & Norman (1998). We find that the redshift variation of the best-fit ST coefficients can be described to very good approximation by a quadratic fit as a function of x given by

$$\begin{cases} A_{200c}(x) = -10.2185312\,x^2 + 4.78051093\,x - 0.1206716 \\ a_{200c}(x) = 4.07275047\,x^2 - 0.49618532\,x + 0.96372361 \\ p_{200c}(x) = -23.48761585\,x^2 + 10.5651697\,x - 1.752599071 \end{cases} \quad (15)$$

$$\begin{cases} A_{500c}(x) = -2.08511667\,x^2 + 2.71726345\,x - 0.59113241 \\ a_{500c}(x) = -1.0788725\,x^2 + 3.25302957\,x - 0.32810261 \\ p_{500c}(x) = 1.04288295\,x^2 - 1.76269479\,x + 0.06162189 \end{cases} \quad (16)$$

and

$$\begin{cases} A_{1000c}(x) = -1.65696205\,x^2 + 3.07836133\,x - 1.20944538 \\ a_{1000c}(x) = -1.18612053\,x^2 + 4.91186256\,x - 1.98337952, \\ p_{1000c}(x) = 1.33135179\,x^2 - 3.7042898\,x + 1.67853762 \end{cases} \quad (17)$$

which we plot in Figure 13 against the best-fit values quoted in Table 4.

In Figure 14 we plot the ST mass functions for M_{200c}, M_{500c}, and M_{1000c} with coefficients given by Equations (15)–(17) against the N-body mass function estimates, which we have referred to as the ST-RayGal mass functions. As we can see, logarithmic deviations with respect to the numerical results are still within the 5% level.

We find that the ST-RayGal mass function formulae can also reproduce the SOD mass functions for M_{500c} and M_{1000c} from N-body simulations with different cosmological parameter values. In particular, we have used halo catalogs at $z = 0$ from simulations of 162 h^{-1} Mpc box length and 512^3 particles of two flat ΛCDM models: ΛCDM-W1 with $\Omega_m = 0.29$, $\sigma_8 = 0.90$, $\Omega_b = 0.047$, and $n_s = 0.990$, and ΛCDM-W5 with $\Omega_m = 0.26$, $\sigma_8 = 0.79$, $\Omega_b = 0.044$, and $n_s = 0.963$. As shown in Figure 15, the logarithmic differences between the ST-RayGal mass function and the numerical estimates from the ΛCDM-W5 and ΛCDM-W1 catalogs are within the 5% level. Using the same halo catalogs, we estimate the average sparsity at $z = 0$. In the case of the ΛCDM-W5 simulation we find $\langle s_{500,1000}\rangle = 1.41$, while in the ΛCDM-W1 case we find $\langle s_{500,1000}\rangle = 1.36$. These values are consistent to within a few percent with the average sparsity prediction inferred by solving Equation (4) with the ST-RayGal mass functions. In particular, we obtain $\langle s^{\rm th}_{500,1000}\rangle = 1.43$ for the ΛCDM-W5 model and $\langle s^{\rm th}_{500,1000}\rangle = 1.39$ for the ΛCDM-W1 cosmology.

ORCID iDs

P. S. Corasaniti https://orcid.org/0000-0002-6386-7846
D. Eckert https://orcid.org/0000-0001-7917-3892

References

Alimi, J.-M., Fűzfa, A., Boucher, V., et al. 2010, MNRAS, 401, 775
Allen, S. W., Evrard, A. E., & Mantz, A. B. 2011, ARA&A, 49, 409
Amodeo, S., Ettori, S., Capasso, R., & Sereno, M. 2016, A&A, 590, A126
Balmes, I., Rasera, Y., Corasaniti, P.-S., & Alimi, J.-M. 2014, MNRAS, 437, 2328
Bhattacharya, S., Habib, S., Heitmann, K., & Vikhlinin, A. 2013, ApJ, 766, 16
Biffi, V., Borgani, S., Murante, G., et al. 2016, ApJ, 827, 112
Bryan, G. L., & Norman, M. L. 1998, ApJ, 495, 80
Bullock, J. S., Kolatt, T. S., & Sigad, Y. 2001, MNRAS, 321, 559
Correa, C. A., Wyithe, J. S. B., Schaye, J., & Duffy, A. R. 2015, MNRAS, 452, 1217
Courtin, J., Rasera, Y., Alimi, J.-M., et al. 2011, MNRAS, 410, 1911
Cyburt, R. H., Fields, B. D., Olive, K. A., & Yeh, T.-H. 2016, RvMP, 88, 015004
de Haan, T., Benson, B. A., Bleem, L. E., et al. 2016, ApJ, 832, 95
Despali, G., Giocoli, C., Angulo, R. E., et al. 2016, MNRAS, 456, 2486
Diemer, B., & Kravtsov, A. V. 2015, ApJ, 799, 108
Dolag, K., Bartelmann, M., Perrotta, F., et al. 2004, A&A, 416, 853
Duffy, A. R., Schaye, J., Kay, S. T., et al. 2010, MNRAS, 405, 2161
Ebeling, H., Edge, A. C., Mantz, A., et al. 2010, MNRAS, 407, 83
Efstathiou, G. 2014, MNRAS, 440, 1138
Eisenstein, D. J., & Hu, W. 1999, ApJ, 496, 605
Ettori, S. 2013, MNRAS, 435, 1265
Ettori, S. 2015, MNRAS, 446, 2629
Ettori, S., Gastaldello, F., Leccardi, A., et al. 2010, A&A, 524, 68
Ettori, S., Ghirardini, V., Eckert, D., Dubath, F., & Pointecouteau, E. 2017, MNRAS, 470, L29
Gelman, A., & Rubin, D. B. 1992, StaSc, 7, 457
Giocoli, C., Tormen, G., & Sheth, R. K. 2012, MNRAS, 422, 185
Hildebrandt, H., Viola, M., Heymans, C., et al. 2017, MNRAS, 465, 1454
Hoekstra, H., Mahdavi, A., Babul, A., & Bildfell, C. 2012, MNRAS, 427, 1298
King, L. J., & Mead, J. M. G. 2011, MNRAS, 416, 2539
Kitayama, T., & Suto, Y. 1996, MNRAS, 280, 638
Klypin, A., Yepes, G., Gottlober, S., Prada, F., & Hess, S. 2016, MNRAS, 457, 4340
Koester, B., McKay, T. A., Annis, J., et al. 2007, ApJ, 660, 221
Komatsu, E., Smith, K. M., Dunkley, J., et al. 2011, ApJS, 192, 18
Kravtsov, A. V., & Borgani, S. 2012, ARA&A, 50, 353
Kwan, J., Sánchez, C., Clampitt, J., et al. 2017, MNRAS, 464, 4045
Lacey, C., & Cole, S. 1994, MNRAS, 271, 676
Le Brun, A. M. C., McCarthy, I. G., Schaye, J., & Ponman, T. J. 2014, MNRAS, 441, 1270
Lewis, A., Challinor, A., & Lasenby, A. 2000, ApJ, 538, 473
Ludlow, A. D., Bose, S., Angulo, R. E., et al. 2016, MNRAS, 460, 1214
Macciò, A. V., Dutton, A. A., Van Den Bosch, F. C., et al. 2007, MNRAS, 378, 55
Mantz, A., Allen, S. W., Ebeling, H., Rapetti, D., & Drlica-Wagner, A. 2010, MNRAS, 406, 1773
Maughan, B. J., Giles, P. A., Randall, S. W., Jones, C., & Forman, W. R. 2012, MNRAS, 421, 1583
McCarthy, I. G., Schaye, J., Ponman, T. J., et al. 2010, MNRAS, 406, 822
Mead, J. M. G., King, L. J., Sijacki, D., et al. 2010, MNRAS, 406, 434
Menanteau, F., Sifòn, C., Barrientos, L. F., et al. 2013, ApJ, 765, 67
Meneghetti, M., & Rasia, E. 2013, arXiv:1303.6158
Meneghetti, M., Rasia, E., Merten, J., et al. 2010, A&A, 514, 93
Merloni, A., Predehl, P., Becker, W., et al. 2011, arXiv:1209.3114
Nagai, D., Vikhlinin, A., & Kravtov, A. 2007, ApJ, 655, 98
Navarro, J. F., Frenk, C. S., & White, S. D. M. 1997, ApJ, 490, 493
Pierre, M., Pacaud, F., Adami, C., et al. 2016, A&A, 592, 16
Piffaretti, R., Arnaud, M., Pratt, G. W., Pointecouteau, E., & Melin, J.-B. 2011, A&A, 534, 109
Pillepich, A., Porciani, C., & Reiprich, T. H. 2012, MNRAS, 422, 44
Planck Collaboration, Ade, P. A. R., et al. 2016a, A&A, 594, A13
Planck Collaboration, Ade, P. A. R., et al. 2016b, A&A, 594, A19
Postman, M., Coe, D., Benítez, N., et al. 2012, Astrophys. J. Suppl., 199, 25
Rasera, Y., Alimi, J.-M., Courtin, J., et al. 2010, in AIP Conf. Proc. 1241, Invisible Universe, ed. J.-M. Alimi & A. Fűzfa (Melville, NY: AIP), 1134
Rasia, E., Meneghetti, M., Martino, R., et al. 2012, NJPh, 14, 055018
Raveri, M., Martinelli, M., Zhao, G., & Wang, Y. 2016a, arXiv:1606.06268
Raveri, M., Martinelli, M., Zhao, G., & Wang, Y. 2016b, arXiv:1606.06273
Reichardt, C. L., Stalder, B., Bleem, L. E., et al. 2013, ApJ, 763, 127
Renneby, M., Hilbert, S., & Angulo, R. 2011, arXiv:1710.03251
Riess, A. G., Macri, L. M., Hoffmann, S. L., et al. 2016, ApJ, 826, 56
Rykoff, E. S., Rozo, E., Busha, M. T., et al. 2014, ApJ, 785, 104
Sarazin, C. L. 1986, RvMP, 58, 1
Schaye, J., Dalla Vecchia, C., Booth, C. M., et al. 2010, MNRAS, 402, 1536
Sereno, M. 2015, MNRAS, 450, 3665
Sereno, M., & Ettori, S. 2015, MNRAS, 450, 3633

Sereno, M., Ettori, S., Giocoli, C., & Moscardini, L. 2015, MNRAS, 449, 2024
Sheth, R. K., & Tormen, G. 1999, MNRAS, 308, 119
Staniszewski, Z., Ade, P. A. R., Aird, K. A., et al. 2009, ApJ, 701, 32
Tinker, J., Kravtsov, A. V., Klypin, A., et al. 2008, ApJ, 688, 709
Umetsu, K., Broadhurst, T., Zitrin, A., et al. 2011, ApJ, 738, 41
Velliscig, M., van Daalen, M., Schaye, J., et al. 2014, MNRAS, 442, 2641
Vikhlinin, A., Markevitch, M., Murray, S. S., Forman, W., & Van Speybroeck, L. 2005, ApJ, 628, 655
Wechsler, R. H., Bullock, J. S., Primack, J. R., Kravtsov, A. V., & Dekel, A. 2002, ApJ, 568, 52
Zhao, D. H., Jing, Y. P., Mo, H. J., & Börner, G. 2003, ApJL, 597, L9
Zhao, D. H., Jing, Y. P., Mo, H. J., & Börner, G. 2009, ApJ, 707, 354